

RESEARCH ARTICLE | FEBRUARY 05 2024

Effect of boron concentration on local structure and spontaneous polarization in AIBN thin films

S. Calderon V ; John Hayden ; M. Delower; Jon-Paul Maria; Elizabeth C. Dickey 



APL Mater. 12, 021105 (2024)

<https://doi.org/10.1063/5.0179942>



CrossMark



APL Energy

Latest Articles Online!

Read Now



Effect of boron concentration on local structure and spontaneous polarization in AlBN thin films

Cite as: APL Mater. 12, 021105 (2024); doi: 10.1063/5.0179942

Submitted: 5 October 2023 • Accepted: 9 January 2024 •

Published Online: 5 February 2024



S. Calderon V,^{1,a)} John Hayden,² M. Delower,² Jon-Paul Maria,² and Elizabeth C. Dickey¹

AFFILIATIONS

¹ Department of Materials Science and Engineering, Carnegie Mellon University, Pittsburgh, Pennsylvania 15213, USA

² Department of Materials Science and Engineering, The Pennsylvania State University, University Park, Pennsylvania 16802, USA

^{a)} Author to whom correspondence should be addressed: scaldero@andrew.cmu.edu

ABSTRACT

The discovery of ferroelectricity in polar wurtzite-based ternary materials, such as $\text{Al}_{1-x}\text{B}_x\text{N}$, has attracted attention due to their compatibility with complementary metal–oxide–semiconductor processes and potential use in integrated non-volatile memory devices. However, the origin of ferroelectricity and the fundamental control of the polarization switching in these materials are still under intensive investigation but appear to be related to local disorder induced from the alloying. In this work, we report the effect of boron alloying on the local structure of $\text{Al}_{1-x}\text{B}_x\text{N}$ films deposited by magnetron sputtering. Our results reveal a diminished crystalline order as a function of boron concentration, accompanied by a reduction in the spontaneous polarization. The film disorder is primarily associated with the dissimilar bond lengths between Al–N and B–N and the formation of threading dislocations induced by B incorporation in the structure.

© 2024 Author(s). All article content, except where otherwise noted, is licensed under a Creative Commons Attribution (CC BY) license (<http://creativecommons.org/licenses/by/4.0/>). <https://doi.org/10.1063/5.0179942>

INTRODUCTION

Wurtzite nitrides have been extensively studied and used in semiconductor devices due to their wide bandgap, high breakdown voltage, and stability.¹ These materials have large spontaneous polarization and exhibit piezoelectric response but have not been conventionally considered to be ferroelectric. AlN, for instance, has been used in optoelectronics, microwave devices, and high-power electronics, thanks to its high thermal conductivity and stability, high electrical resistivity, and large bandgap. In 2009, Akiyama *et al.*² showed a fivefold enhancement in the piezoelectric response by alloying AlN with Sc, and since then, different alloying elements have been evaluated as possible candidates to enhance the piezoelectric response of AlN.³ Most recently, ferroelectricity at room temperature was demonstrated in high-alloy content $\text{Al}_{1-x}\text{Sc}_x\text{N}$ ⁴ and $\text{Al}_{1-x}\text{B}_x\text{N}$,⁵ as evidenced by hysteretic and well-saturated PE loops,^{4,5} as well as by the switching behavior in piezoresponse force microscopy⁶ and scanning transmission electron microscopy.⁷ The Sc or B alloying concentration controls the coercive field and magnitude of the spontaneous polarization. As a result of these properties and the processing compatibility with the complementary metal–oxide–semiconductor (CMOS), AlN has emerged as a candidate for integration in the

semiconductor industry for sensor, actuators, non-volatile memory integration, etc.

The most intensive experimental research has been carried out on $\text{Al}_{1-x}\text{Sc}_x\text{N}$, since ferroelectricity was first demonstrated in this alloy by Fichtner *et al.*⁴ $\text{Al}_{1-x}\text{Sc}_x\text{N}$ has been investigated to understand the effect of deposition conditions, phases, crystallinity, crystal quality, etc., on the ferroelectric properties.^{8–19} Increasing Sc concentration in epitaxial $\text{Al}_{1-x}\text{Sc}_x\text{N}$ has been shown to decrease the crystalline order and eventually induce precipitation of the rock salt structure for Sc content >30 at.%.¹⁵ Local structure and defect densities have been shown to play a significant role in the performance of $\text{Al}_{1-x}\text{Sc}_x\text{N}$ films, where the leakage current and breakdown strength are improved by decreasing the dislocation density in the film.²⁰ The coercive field and remanent polarization depend on the Sc concentration, with the largest switchable polarization higher than $100 \mu\text{C cm}^{-2}$.⁴ In addition, Lee *et al.*²¹ have computationally shown that increasing the chemical complexity, by increasing the Sc content, alters the switching mechanisms in $\text{Al}_{1-x}\text{Sc}_x\text{N}$. However, more research is required to understand the effects of structural features on the switchability and spontaneous polarization in these ternary nitrides. Some studies suggest that the c/a ratio substantially contributes to the polarization reversal via lattice strain;²² however, recent studies show that the ferroelectricity in $\text{Al}_{1-x}\text{Sc}_x\text{N}$ films is also

affected by the chemical bonding and local distortions caused by Sc incorporation.¹⁰

Even less is known about the effects of B alloying on the local structure in $\text{Al}_{1-x}\text{B}_x\text{N}$ ferroelectric thin films, which maintains a higher bandgap relative to $\text{Al}_{1-x}\text{Sc}_x\text{N}$ films. Furthermore, relative to Sc, B is cheaper and has a lower supply-chain risk. Density functional theory (DFT) calculations have shown significant differences regarding the most favorable switching pathways for both $\text{Al}_{1-x}\text{Sc}_x\text{N}$ and $\text{Al}_{1-x}\text{B}_x\text{N}$,²³ which may indicate different substituent effects on the structural characteristics. Zagorac *et al.*, using first-principles simulations, showed that wurtzite remains the most energetically favorable structure over the composition range $0.125 \leq x \leq 0.375$ in $\text{Al}_{1-x}\text{B}_x\text{N}$,²⁴ whereas Liu *et al.* later calculated that wurtzite stability remains only up to 19% B.²³ Experimental studies show that B incorporation leads to smaller lattice parameters in sputtered thin films,^{5,25} but more research is necessary to understand the effects of deposition conditions on the presence of phases, defects, crystal quality, interfaces, and their ferroelectric behavior to better design $\text{Al}_{1-x}\text{B}_x\text{N}$ films ready for CMOS technology integration.

Consequently, to better understand the effect of boron concentration on the structural properties, we report a detailed characterization of $\text{Al}_{1-x}\text{B}_x\text{N}$ ($x = 0, 6, 13$, and 20 at. %) films deposited by magnetron sputtering. Structural analysis is carried out by conventional and scanning transmission electron microscopies, where the evolution of defects and spontaneous polarization is evaluated as a function of boron content.

MATERIALS AND METHODS

$\text{Al}_{1-x}\text{B}_x\text{N}$ films of 250–500 nm thickness are deposited on 100 nm epitaxially grown (110) W electrodes on (0001) sapphire substrates. The substrate temperature is maintained at 400°C for the deposition of the bottom electrode and $\text{Al}_{1-x}\text{B}_x\text{N}$ layers. The thermal budget is maintained at 400°C or below such that the process is CMOS back-end-of-the-line compatible. $\text{Al}_{1-x}\text{B}_x\text{N}$ films are deposited by simultaneous reactive pulsed dc sputtering from a 2 in. Al (99.9995%, Kurt J. Lesker) target and rf sputtering from a 2 in. BN (99.5%, Kurt J. Lesker) target in a mixed nitrogen and argon atmosphere at 0.227 Pa flowing at 10 SCCM Ar and 10 SCCM N_2 . The pulsed dc parameters for the Al source are kept constant at 100 kHz and 1536 ns pulse width with a time-averaged power of 200 W.

The B concentration in the films is controlled by modulating the BN target power from 0 to 150 W and is measured by x-ray photoelectron spectroscopy (XPS) using a Physical Electronics VersaProbe II. High-resolution spectra of the B 1s and Al 2p orbitals are collected and integrated using linear and Shirley backgrounds, respectively. Multiple scans of the low-intensity B 1s peak are recorded and averaged together to improve the signal-to-noise ratio. Integrated area ratios normalized with relative sensitivity factors from the CasaXPS software package are then used to calculate the B concentration in the films using the formula $x = [\text{B}]/([\text{Al}] + [\text{B}])$.

TEM images are acquired from mechanically polished and Ar ion-thinned samples, using a Thermo Fisher Titan-ThemisTM STEM operated at 200 kV. Conventional bright field (BF) TEM and centered dark field (DF) images are acquired on a Thermo ScientificTM

CetaTM camera. STEM images are acquired using a four-segment annular detector (DF4) in the differential phase contrast (DPC) mode to image N and Al simultaneously. Samples are crystallographically aligned with the detector segments to reduce errors in the determination of the atomic column position.²⁶ Differentiated DPC (dDPC) images are calculated as the gradient of the DPC signal. A probe convergence angle of 17.9 mrad and a camera length that results in acceptance angles between 11 and 43 mrad are used. A set of 20 frames is collected using 200 ns dwell time and registered by cross correlation to correct for specimen drift that can cause distortions in the images.

Position-averaged convergent beam electron diffraction (PACBED) patterns are acquired with a probe convergence angle of 17.9 mrad from a region with at least 200 $\text{Al}_{1-x}\text{B}_x\text{N}$ projected unit cells. The sample thickness is then estimated by comparing the experimental and simulated PACBED patterns, using the same experimental conditions (see Fig. S1). Multislice image simulations using abTEM²⁷ are used to simulate PACBED patterns with ten variants in the frozen phonon configuration at 200 keV with a spherical aberration of 1 μm , varying the sample thickness.

N–Al vector pair correlation functions (vPCFs) are calculated using the Single Origin Python library, as described elsewhere.²⁸ Briefly, atomic column positions are located from an atomic-resolved STEM image, fitted with non-circular 2D-Gaussians, and divided into Al and N sublattices. The atomic columns are fitted with two Gaussians simultaneously as dumbbell features due to the proximity of Al and N when observed along the [110] direction, ensuring that the effect of the nearby atomic-column intensity is taken into consideration. A 2D-histogram with the N-atomic-column to Al-atomic-column distances and directions is plotted, as illustrated from the simulated data shown in Fig. 1. N-atomic column positions are represented by the origin of the vPCF, shown as a yellow circle in Fig. 1(a). A vector from the origin to the center of mass of any vPCF peak indicates an average distance and direction from the N-atomic column to the Al-atomic column in the structure, as shown in Figs. 1(b) and 1(c). On the other hand, the distribution of the peaks in the vPCF represents the vector variations in the region where the vPCF was calculated, providing information about local order/disorder.

The average lattice parameters and spontaneous polarization²⁹ are calculated based on the vPCF, as shown in Fig. 1(a). \vec{r} represents the mean displacement vector of the cations relative to the anions along the [001] direction, which is used to calculate the polarization per unit cell, based on the following equation:

$$\Delta P = 2 \frac{e}{\Omega} Z_{\text{Al}}^* \vec{r}, \quad (1)$$

where ΔP is the change in polarization from a centrosymmetric h-BN reference phase, e is the positive electronic charge, Ω is the unit cell volume, and Z_{Al}^* is the Born effective charge for the Al atom. Notice that $\vec{r} = 0$ for a centrosymmetric hexagonal AlN structure; hence, ΔP can be interpreted as spontaneous polarization. The c lattice parameter is extracted from the vPCF as twice the distance between two Al atomic columns along the [001] direction ($2 \cdot d_{002}$), while a is calculated as $d_{1\bar{1}0} = a \cdot \cos(30^\circ)$, where $d_{1\bar{1}0}$ is the distance between two Al atomic columns along the $[1\bar{1}0]$ direction. Then, Ω is calculated as $\Omega = a^2 c \cdot \cos(30^\circ)$.

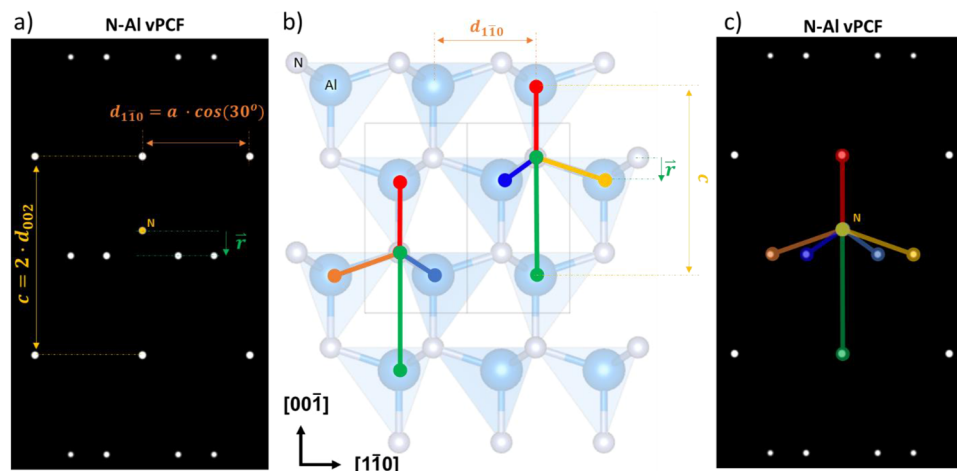


FIG. 1. (a) 2D-vPCF for N-Al, in which the interatomic distances to determine the lattice parameter (a and c) and the mean displacement between Al and N along the $[001]$ direction (r) are indicated, (b) atomic model projected along the $[110]$ direction, and (c) 2D-vPCF for N-Al, in which the colored lines indicate the atomic-column distances in the atomic model (b).

Density functional theory calculations are conducted using the Vienna *Ab initio* Simulation Package (VASP) using the projected augmented wave method, employing the generalized gradient approximation and following the Perdew–Burke–Ernzerhof (PBE) parameterization for exchange–correlation electronic interactions.^{30–32} To investigate the influence of boron substitution on the polarization properties of AlN, a 72-atom supercell is constructed, which enables the exploration of the relevant $\text{Al}_{1-x}\text{B}_x\text{N}$ compositions. The boron atoms are randomly distributed within the supercell using the protocol in the special quasi-random structure (SQS) generation module of the Alloy Theoretic Automated Toolkit (ATAT) package.³³ The energy cutoff is set to 520 eV, and a $2 \times 2 \times 2$ k-point grid based Monkhorst–Pack scheme is used for calculations. More details of the calculation procedures can be found in Ref. 5.

RESULTS AND DISCUSSION

A summary comparison of the structural and morphological features observed by conventional TEM is shown in Fig. 2. Selected area diffraction patterns from $\text{Al}_{1-x}\text{B}_x\text{N}$ as a function of boron content are shown in the insets of Fig. 2. The patterns show the orientation relationship between the sapphire substrate, the tungsten electrode, and the films as $(001)_S // (110)_W // (001)_{\text{AlBN}}$ (see Fig. S2). For low boron contents, the epitaxial growth is maintained along the thickness [Figs. 2(a)–2(c)]. However, for the largest B content (20 at. %), the epitaxial growth is lost after ~ 100 nm, and a randomly oriented polycrystalline growth is observed, as shown in Fig. 2(d). No evidence of a secondary phase is observed within the B concentration range studied in this report. This is consistent with DFT calculations reported by Liu *et al.*,²³ which show that the wurtzite structure is the most stable phase in $\text{Al}_{1-x}\text{B}_x\text{N}$ for B contents up to 19 at. %. Furthermore, Zagorac *et al.*²⁴ calculated that under ambient conditions, wurtzite is the most energetically

favorable structure at standard pressure for B concentrations up to 37.5 at. %.

Figure 2 shows the cross-sectional on-axis bright field (BF) and dark field (DF) TEM images for $\text{Al}_{1-x}\text{B}_x\text{N}$ for different boron contents, $x = 0, 0.06, 0.13$, and 0.20 . The figures show a columnar growth, where the lateral grain size changes as a function of boron content with a concomitant increase in the dislocation defect density. To further characterize the defects, two diffraction conditions are used to acquire the DF images, namely $g = [002]$ (i.e., g_{002}) and g orthogonal to g_{002} . The images reveal a higher density of defects for larger boron contents independent of the diffraction condition selected. DF images using the g_{002} vectors show linear features that are perpendicular to the surface of the substrate [see Figs. 2(e)–2(h)], characteristic of threading dislocations, as observed for similar structures.³⁴ DF images acquired using a g vector perpendicular to g_{002} show a more granular morphology. The dominant dislocations reported in the wurtzite structure, such as GaN,³⁵ are screw dislocations defined by the Burgers vector, $b = \langle 001 \rangle$, and edge dislocations with $b = 1/3 \langle 110 \rangle$. Mixed threading dislocations also occur frequently and can be decomposed in edge and screw components. It is worth noting that the higher defect densities occur at the interface with the W electrode in all films. The dense defect region is observed within the first 100 nm of film from the substrate, which indicates the annihilation of the threading dislocation as a function of thickness, as previously modeled.³⁶ A high density of threading dislocation can deteriorate the electrical performance of the films, especially for screw threading dislocations,³⁷ and increase the leakage currents, in agreement that these films exhibit a high insulation resistance up to $\sim 6\%$ B, above which the leakage current values increase, consistent with the increased defect concentration and structural disorder occurring in this range. It is important to note that changes in B concentration are attained by altering the deposition conditions, which may modify the plasma energy, local strain, and ion bombardment, among others. Thus, combinations of

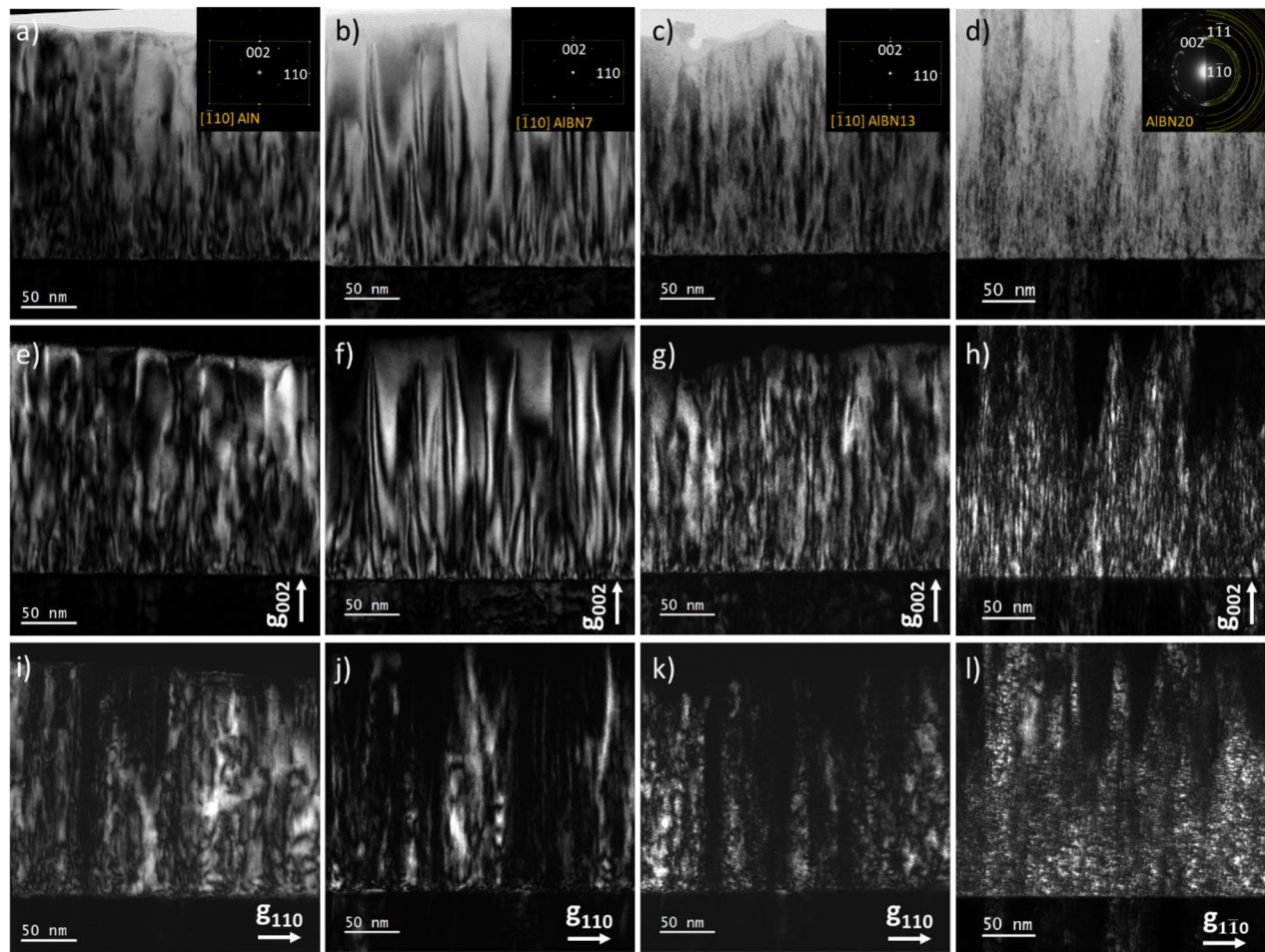


FIG. 2. Cross-sectional on-axis bright field TEM images for $\text{Al}_{1-x}\text{B}_x\text{N}$ with x equal to (a) 0, (b) 0.06, (c) 0.13, and (d) 0.20. The insets in panels (a)–(d) are the corresponding selected area electron diffraction patterns. The yellow lines highlight the $\text{Al}_{1-x}\text{B}_x\text{N}$ reflection to differentiate them from the substrate and W electrode. The corresponding dark field TEM images for g_{002} vector for $x = 0$ (e), 0.06 (f), 0.13 (g), and 0.20 (h). The corresponding dark field images for a g vector orthogonal to g_{002} for $x = 0$ (i), 0.06 (j), 0.13 (k), and 0.20 (l).

these effects, together with the changes in the local structure, caused by the B concentration are possible contributors to the $\text{Al}_{1-x}\text{B}_x\text{N}$ defect density and disorder.

To further quantify the disorder that emerges in the highest B-content $\text{Al}_{0.8}\text{B}_{0.2}\text{N}$ film and its thickness dependence, 4D STEM analysis is carried out. Figure S3 shows the epitaxial growth near the substrate for the first 100 nm, transitioning to misoriented grains for larger thicknesses. Any grains with $[001]$ tilted off the substrate normal will experience a smaller electric field component parallel to the polar axis for a given voltage, which will make switching more difficult, particularly in systems where coercive voltages are close to the breakdown voltages. Previous studies have demonstrated that high B-content films with a similar disorder do not show polarization reversal.⁵ This additional analysis is included to demonstrate that highly metastable compositions with 20% B can be experimentally achieved, likely from quenching the high kinetic energy of

sputtered adatoms and interface epitaxy contributions. However, this state may be difficult to sustain to arbitrary thickness values. In addition, it is important to note that the $\sim 20\%$ limit reported here is likely not universal, i.e., the width of the solubility window achievable by magnetron sputtering may depend on deposition energetics and the substrate choice, among other factors.

Atomic resolution images are acquired to determine the local structural changes caused by the boron incorporation. Figures 3(a)–3(d) show the dDPC-STEM images for $\text{Al}_{1-x}\text{B}_x\text{N}$ along the $[110]$ zone axis, with different boron contents $x = 0, 0.06, 0.13$, and 0.20. Although less disordered regions are selected for atomic resolution in all compositions, the images evidence a higher content of defects for the 13 and 20 at. % of boron-concentration films, in agreement with highly defective films observed by the DF images (see Figure. S4 for a larger field of view).

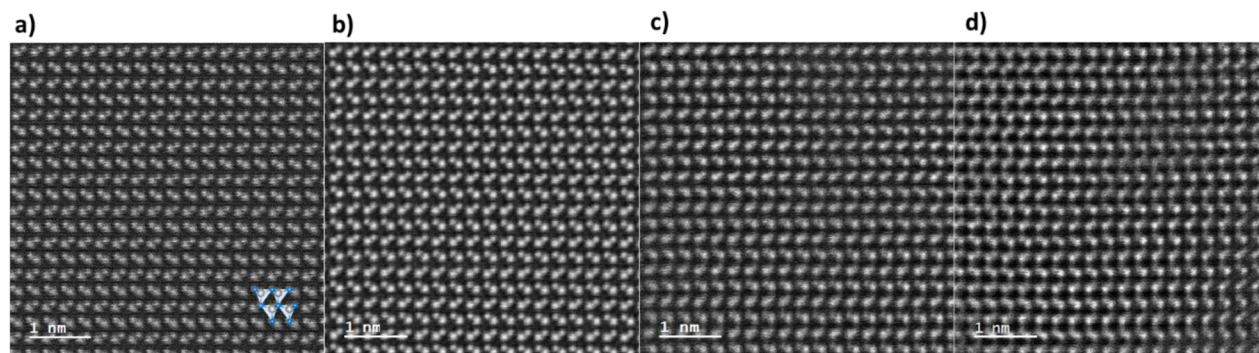


FIG. 3. STEM-dDPC images for $\text{Al}_{1-x}\text{B}_x\text{N}$ with x equal to (a) 0, (b) 0.06, (c) 0.13, and (d) 0.20.

Film growth exhibits an N-polar orientation [see Fig. 3(a), inset] independent of the boron content. N-Al vector pair-correlation functions (vPCFs), calculated from Figs. 3(a)–3(d), are shown in Fig. 4. For clarity, the origin of the vPCF is marked with a yellow circle, which represents the position of the N-atomic columns, while the vPCF peak intensities represent the distribution of the N-Al bonds projected along the [110] direction. To correlate the experimental results and modeled structures, vPCFs are also calculated from the projected atomic positions of the relaxed SQS models with similar compositions, projected along the [110]

zone axis. Both experimental and simulated results evidence larger structural dispersions as boron is incorporated. This is attributed to the significant changes in the local bonding due to the smaller bond length of B-N (≈ 1.60 Å) compared to Al-N (≈ 1.91 Å), as observed in the SQS relaxed models, promoting local disorder. Although both c and a lattice parameters have been shown to decrease monotonically as a function of B content maintaining a c/a ratio of 1.6,⁵ the vPCF standard deviation (i.e., 0.1 Å) lies within the variation range, which hinders the observation of such small changes. However, the c/a ratio of 1.60 ± 0.02 is observed among

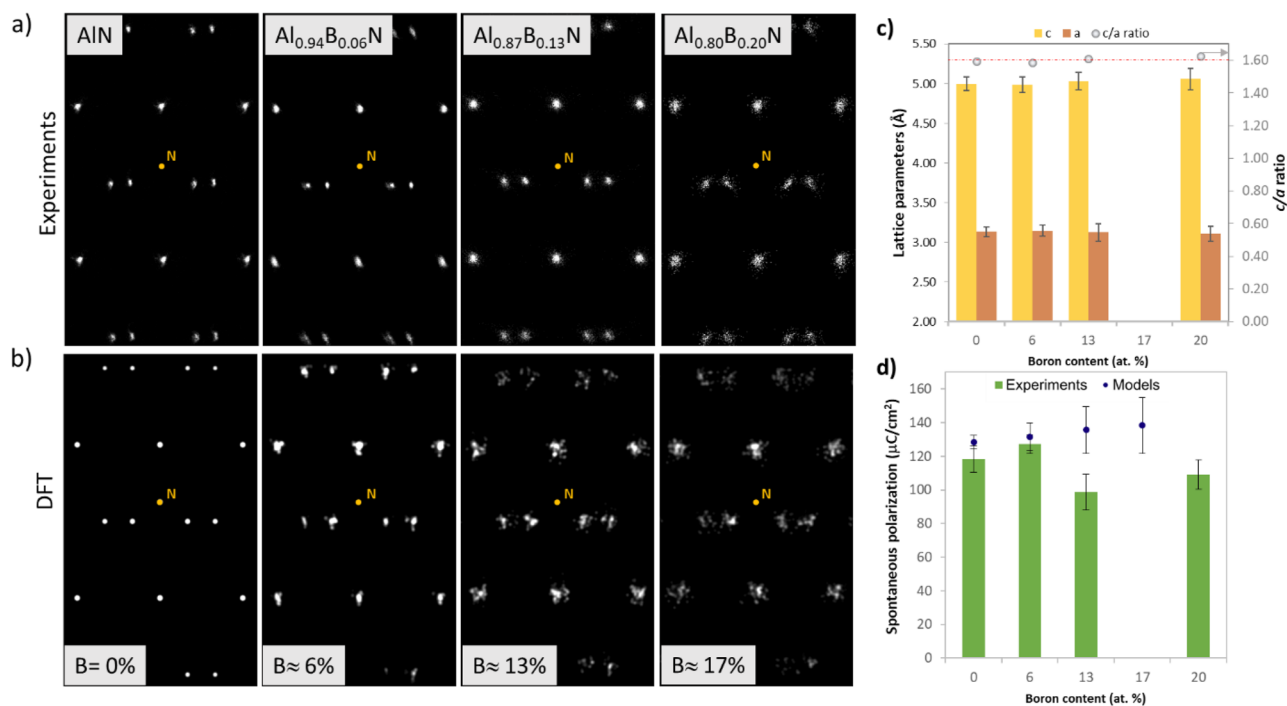


FIG. 4. (a) Experimental 2D N-Al(B) vector pair correlation function for $\text{Al}_{1-x}\text{B}_x\text{N}$ with $x = 0, 0.06, 0.13$, and 0.20 . (b) 2D vector pair correlation function for N-Al and N-B for 0%, 6%, 13, and 17 at. % of B in AlBN from DFT models, (c) lattice parameters and c/a ratio, and (d) structure-based polarization calculated from vPCFs.

different compositions [see Fig. 4(c)], in agreement with previous reports.

Figure 4(d) shows the structure-based spontaneous polarization calculated from the vPCF, indicating a slight increase from $118 \pm 8 \mu\text{C}/\text{cm}^2$ in pure AlN to $128 \pm 6 \mu\text{C}/\text{cm}^2$ for 6 at. % boron, while decreasing for higher boron contents. Structure-based spontaneous polarization was also calculated from the DFT models. The DFT-based calculations predict a monotonic increase in polarization as a function of boron content. Such discrepancies between experiment and theory are attributed to an overall decrease in crystalline order with an increase in B concentration, which is not accounted for in the DFT calculations. Hayden *et al.*⁵ also reported decreasing remanent polarization values obtained by P–E hysteresis loops in $\text{Al}_{1-x}\text{B}_x\text{N}$, demonstrating similar tendencies to the structure-based spontaneous polarization measurements. In this study, the authors attribute the diminishing value of the remanent polarization for B contents that are larger than 6 at. % to a reduced crystallinity and to an increase in in- and out-of-plane mosaicity.

CONCLUSIONS

$\text{Al}_{1-x}\text{B}_x\text{N}$ films (with $0 \leq x \leq 0.2$) deposited on W/sapphire substrates using magnetron sputtering were investigated by transmission electron microscopy. Cross-sectional images revealed a typical columnar growth of the films, with a high density of threading dislocations that increase as a function of the boron content. A reduction in the crystalline order is observed for larger contents of boron, to a point at which the epitaxial growth is compromised and a random orientation evolves as a function of thickness for $\text{Al}_{0.8}\text{B}_{0.2}\text{N}$ films. Structural analysis by vPCFs showed that the *c/a* lattice parameter ratio remained constant at around 1.60, while providing information in the local disorder from the spread in the peak distributions. These vPCF distributions broadened substantially with the addition of B to the AlN lattice. Spontaneous polarization in the films varied from 99 ± 10 to $128 \pm 6 \mu\text{C}/\text{cm}^2$, with a maximum at 6 at. % B, attributed to the local increase in the Al–(N,B) bond lengths attendant with the B alloying. Beyond 6 at. % B, we note a decrease in spontaneous polarization, which is attributed to a greater crystalline disorder in the films.

SUPPLEMENTARY MATERIAL

The supplementary material provides the additional simulated PACBED patterns for AlN as a function of thickness and crystal mistilt, SAED patterns for AlN, 4DSTEM analysis of the $\text{Al}_{0.8}\text{B}_{0.2}\text{N}$ layer, and larger field of view STEM-dDPC atomic resolution images for $\text{Al}_{1-x}\text{B}_x\text{N}$.

ACKNOWLEDGMENTS

This material is based upon the work supported by the center for 3D Ferroelectric Microelectronics (3DFeM), an Energy Frontier Research Center funded by the U.S. Department of Energy, Office of Science, Office of Basic Energy Sciences Energy Frontier Research Centers program under Award No. DE-SC0021118. E.C.D. and S.C.

acknowledge the use of the Materials Characterization Facility at Carnegie Mellon University supported by Grant No. MCF-677785.

AUTHOR DECLARATIONS

Conflict of Interest

The authors have no conflicts to disclose.

Author Contributions

S. Calderon V: Conceptualization (equal); Formal analysis (equal); Investigation (equal); Methodology (equal); Writing – original draft (equal); Writing – review & editing (equal). **John Hayden:** Investigation (equal); Writing – review & editing (equal). **M. Delower:** Investigation (equal); Writing – review & editing (equal). **Jon-Paul Maria:** Funding acquisition (equal); Investigation (equal); Supervision (equal); Writing – review & editing (equal). **Elizabeth C. Dickey:** Conceptualization (equal); Funding acquisition (equal); Methodology (equal); Supervision (equal); Writing – review & editing (equal).

DATA AVAILABILITY

The data that support the findings of this study are available from the corresponding author upon reasonable request.

REFERENCES

- H. Morkoç, S. Strite, G. B. Gao, M. E. Lin, B. Sverdlov, and M. Burns, “Large-band-gap SiC, III-V nitride, and II-VI ZnSe-based semiconductor device technologies,” *J. Appl. Phys.* **76**(3), 1363–1398 (1994).
- M. Akiyama, T. Kamohara, K. Kano, A. Teshigahara, Y. Takeuchi, and N. Kawahara, “Enhancement of piezoelectric response in scandium aluminum nitride alloy thin films prepared by dual reactive cosputtering,” *Adv. Mater.* **21**(5), 593–596 (2009).
- J. Startt, M. Quazi, P. Sharma, I. Vazquez, A. Poudyal, N. Jackson, and R. Dingreville, “Unlocking AlN piezoelectric performance with earth-abundant dopants,” *Adv. Electron. Mater.* **9**(4), 2201187 (2023).
- S. Fichtner, N. Wolff, F. Lofink, L. Kienle, and B. Wagner, “AlScN: A III-V semiconductor based ferroelectric,” *J. Appl. Phys.* **125**(11), 114103 (2019).
- J. Hayden, M. D. Hossain, Y. Xiong, K. Ferri, W. Zhu, M. V. Imperatore, N. Giebink, S. Trolrier-McKinstry, I. Dabo, and J.-P. Maria, “Ferroelectricity in boron-substituted aluminum nitride thin films,” *Phys. Rev. Mater.* **5**(4), 044412 (2021).
- D. Wang, P. Wang, S. Mondal, S. Mohanty, T. Ma, E. Ahmadi, and Z. Mi, “An epitaxial ferroelectric ScAlN/GaN heterostructure memory,” *Adv. Electron. Mater.* **8**(9), 2200005 (2022).
- S. Calderon, J. Hayden, S. M. Baksa, W. Tzou, S. Trolrier-McKinstry, I. Dabo, J.-P. Maria, and E. C. Dickey, “Atomic-scale polarization switching in wurtzite ferroelectrics,” *Science* **380**(6649), 1034–1038 (2023).
- P. Wang, D. Wang, Y. Bi, B. Wang, J. Schwartz, R. Hovden, and Z. Mi, “Quaternary alloy ScAlGaN: A promising strategy to improve the quality of ScAlN,” *Appl. Phys. Lett.* **120**(1), 012104 (2022).
- J. Su, S. Fichtner, M. Z. Ghori, N. Wolff, M. R. Islam, A. Lotnyk, D. Kaden, F. Niekel, L. Kienle, B. Wagner, and F. Lofink, “Growth of highly c-axis oriented AlScN films on commercial substrates,” *Micromachines* **13**(5), 783 (2022).
- K. Yazawa, J. S. Mangum, P. Gorai, G. L. Brennecke, and A. Zakutayev, “Local chemical origin of ferroelectric behavior in wurtzite nitrides,” *J. Mater. Chem. C* **10**(46), 17557–17566 (2022).

- ¹¹C. Liu, Q. Wang, W. Yang, T. Cao, L. Chen, M. Li, F. Liu, D. K. Loke, J. Kang, and Y. Zhu, in *2021 IEEE International Electron Devices Meeting IEDM* (IEEE, San Francisco, CA, 2021), pp. 8.1.1–8.1.4.
- ¹²G. Schönweger, M. R. Islam, N. Wolff, A. Petraru, L. Kienle, H. Kohlstedt, and S. Fichtner, “Ultrathin $\text{Al}_{1-x}\text{Sc}_x\text{N}$ for low-voltage-driven ferroelectric-based devices,” *Phys. Status Solidi RRL* **17**(1), 2200312 (2023).
- ¹³C. Liu, M. Li, B. Chen, Y. Zhang, Y. Zhu, and N. Wang, “Evaluation of the impact of abnormal grains on the performance of $\text{Sc}_{0.15}\text{Al}_{0.85}\text{N}$ -based BAW resonators and filters,” *J. Micromech. Microeng.* **32**(3), 034002 (2022).
- ¹⁴D. Wang, J. Zheng, Z. Tang, M. D’Agati, P. S. M. Gharavi, X. Liu, D. Jariwala, E. A. Stach, R. H. Olsson, V. Roebisch, M. Kratzer, B. Heinz, M.-G. Han, and K. Kisslinger, in *2020 Joint Conference of the IEEE International Frequency Control Symposium and IEEE International Symposium on Applications of Ferroelectrics IFCS-ISAF* (IEEE, Keystone, CO, 2020), pp. 1–4.
- ¹⁵X. Zhang, E. A. Stach, W. J. Meng, and A. C. Meng, “Nanoscale compositional segregation in epitaxial AlScN on Si (111),” *Nanoscale Horiz.* **8**(5), 674–684 (2023).
- ¹⁶M. R. Islam, N. Wolff, M. Yassine, G. Schönweger, B. Christian, H. Kohlstedt, O. Ambacher, F. Lofink, L. Kienle, and S. Fichtner, “On the exceptional temperature stability of ferroelectric $\text{Al}_{1-x}\text{Sc}_x\text{N}$ thin films,” *Appl. Phys. Lett.* **118**(23), 232905 (2021).
- ¹⁷R. Guido, P. D. Lomenzo, M. R. Islam, N. Wolff, M. Gremmel, G. Schönweger, H. Kohlstedt, L. Kienle, T. Mikolajick, S. Fichtner, and U. Schroeder, “Thermal stability of the ferroelectric properties in 100 nm-thick $\text{Al}_{0.72}\text{Sc}_{0.28}\text{N}$,” *ACS Appl. Mater. Interfaces* **15**(5), 7030–7043 (2023).
- ¹⁸D. Drury, K. Yazawa, A. Mis, K. Talley, A. Zakutayev, and G. L. Brennecke, “Understanding reproducibility of sputter-deposited metastable ferroelectric wurtzite $\text{Al}_{0.6}\text{Sc}_{0.4}\text{N}$ films using in situ optical emission spectrometry,” *Phys. Status Solidi RRL* **15**(5), 2100043 (2021).
- ¹⁹G. Schönweger, A. Petraru, M. R. Islam, N. Wolff, B. Haas, A. Hammud, C. Koch, L. Kienle, H. Kohlstedt, and S. Fichtner, “From fully strained to relaxed: Epitaxial ferroelectric $\text{Al}_{1-x}\text{Sc}_x\text{N}$ for III-N technology,” *Adv. Funct. Mater.* **32**(21), 2109632 (2022).
- ²⁰D. Wang, P. Wang, S. Mondal, Y. Xiao, M. Hu, and Z. Mi, “Impact of dislocation density on the ferroelectric properties of ScAlN grown by molecular beam epitaxy,” *Appl. Phys. Lett.* **121**(4), 042108 (2022).
- ²¹C.-W. Lee, K. Yazawa, A. Zakutayev, G. L. Brennecke, and P. Gorai, *Switching it Up: New Mechanisms Revealed in Wurtzite-Type Ferroelectrics* (Chemistry, 2023).
- ²²S. Yasuoka, R. Mizutani, R. Ota, T. Shiraishi, T. Shimizu, M. Uehara, H. Yamada, M. Akiyama, and H. Funakubo, “Tunable ferroelectric properties in wurtzite $(\text{Al}_{0.8}\text{Sc}_{0.2})\text{N}$ via crystal anisotropy,” *ACS Appl. Electron. Mater.* **4**(11), 5165–5170 (2022).
- ²³Z. Liu, X. Wang, X. Ma, Y. Yang, and D. Wu, “Doping effects on the ferroelectric properties of wurtzite nitrides,” *Appl. Phys. Lett.* **122**(12), 122901 (2023).
- ²⁴D. Zagorac, J. Zagorac, M. Fonović, T. Prikhna, and B. Matović, “Novel boron-rich aluminum nitride advanced ceramic materials,” *Int. J. Appl. Ceram. Technol.* **20**(1), 174–189 (2023).
- ²⁵L. Liljeholm and J. Olsson, “Electrical characterization of wurtzite $(\text{Al,B})\text{N}$ thin films,” *Vacuum* **86**(4), 466–470 (2011).
- ²⁶S. Calderon and E. C. Dickey, “Structural modification in B-doped AlN ferroelectric films by STEM-DPC,” *Microsc. Microanal.* **29**(Supplement_1), 1796–1797 (2023).
- ²⁷J. Madsen and T. Susi, “The abTEM code: Transmission electron microscopy from first principles,” *Open Res. Eur.* **1**, 24 (2021).
- ²⁸S. D. Funni, Z. J. Yang, M. J. Cabral, C. Ophus, X. M. Chen, and E. C. Dickey, “Theory and application of the vector pair correlation function for real-space crystallographic analysis of order/disorder correlations from STEM images,” *APL Mater.* **9**(9), 091110 (2021).
- ²⁹R. D. King-Smith and D. Vanderbilt, “Theory of polarization of crystalline solids,” *Phys. Rev. B* **47**(3), 1651–1654 (1993).
- ³⁰J. P. Perdew, K. Burke, and M. Ernzerhof, “Generalized gradient approximation made simple,” *Phys. Rev. Lett.* **77**(18), 3865–3868 (1996).
- ³¹G. Kresse and J. Furthmüller, “Efficient iterative schemes for *ab initio* total-energy calculations using a plane-wave basis set,” *Phys. Rev. B* **54**(16), 11169–11186 (1996).
- ³²G. Kresse and D. Joubert, “From ultrasoft pseudopotentials to the projector augmented-wave method,” *Phys. Rev. B* **59**(3), 1758–1775 (1999).
- ³³A. Van De Walle, M. Asta, and G. Ceder, “The alloy theoretic automated toolkit: A user guide,” *Calphad* **26**(4), 539–553 (2002).
- ³⁴C. J. Lu, L. A. Bendersky, H. Lu, and W. J. Schaff, “Threading dislocations in epitaxial InN thin films grown on (0001) sapphire with a GaN buffer layer,” *Appl. Phys. Lett.* **83**(14), 2817–2819 (2003).
- ³⁵S. K. Mathis, A. E. Romanov, L. F. Chen, G. E. Beltz, W. Pompe, and J. S. Speck, “Modeling of threading dislocation reduction in growing GaN layers,” *J. Cryst. Growth* **231**(3), 371–390 (2001).
- ³⁶T. Ward, A. M. Sánchez, M. Tang, J. Wu, H. Liu, D. J. Dunstan, and R. Beanland, “Design rules for dislocation filters,” *J. Appl. Phys.* **116**(6), 063508 (2014).
- ³⁷Y. Yamaoka, A. Ubukata, Y. Yano, T. Tabuchi, K. Matsumoto, and T. Egawa, “Effect of threading dislocation in an AlN nucleation layer and vertical leakage current in an AlGaIn/GaN high-electron mobility transistor structure on a silicon substrate,” *Semicond. Sci. Technol.* **34**(3), 035015 (2019).